PERGAMON

Journal of Atmospheric and Solar-Terrestrial Physics 65 (2003) 59–70

Journal of ATMOSPHERIC AND SOLAR-TERRESTRIAL PHYSICS

www.elsevier.com/locate/jastp

Wave structures in the electron density profile in the ionospheric D- and E-layers observed by radio holography analysis of the GPS/MET radio occultation data

A. Pavelyev[a,d,*], T. Tsuda[a], K. Igarashi[b], Y.A. Liou[c], K. Hocke[b]

[a] *Radio Science Center for Space and Atmosphere, RASC, Gokasho, Uji, Kyoto 611-011, Japan*
[b] *Communications Research Laboratory, Ministry of Posts and Telecommunications, 4-2-1, Nukui-Kita Machi, Koganei-shi, Tokyo 184-8795, Japan*
[c] *Center for Space and Remote Sensing Research, National Central University, Chung-Li 320, Taiwan*
[d] *Institute of Radio Engineering and Electronics of Russian Academy of Sciences, (IRE RAS), Fryazino, Vvedenskogo sq. 1, 141120 Moscow region, Russia*

Received 11 May 2001; received in revised form 8 July 2002; accepted 23 July 2002

Abstract

Vertical distribution of the electron density in the upper atmosphere can be studied using high-precision global positioning system (GPS). In this paper, we show that the radio holography method allows one to determine the vertical profile of the electron density and monitoring wave structures in the upper atmosphere. As an example of this approach, results of analysis of data corresponding to four GPS/Meteorology (GPS/MET) radio occultation events are presented. The radio holograms of the D-layer of the ionosphere reconstructed from radio occultation data revealed wave structures with vertical scales of about 1–8 km and variations in the vertical gradient of the electron density from $\pm 5 \times 10^3$ to $\pm 8 \times 10^3$ electrons/(cm^3 km) at altitudes of 72–95 km. These structures may be caused by wind shear and atmospheric internal waves with vertical scales ranging from a few hundred meters to several kilometers, which produce vertical convergence of the plasma velocity and plasma advection. Theoretical consideration shows a possibility of qualitative determination of the vertical gradient of the horizontal wind velocity in the E-layer and estimation of the temperature variations in the neutral gas in the D-layer region from observed profiles of the electron density. Variations in the electron density are connected with the temperature changes. The connection coefficient depends on the vertical velocity of the neutral gas motion in the mesosphere. Maximums of the temperature deviation correspond to those in the electron density profile. The results indicate a possibility to estimate the form of the small-scale temperature vertical perturbations in the mesosphere using the radio occultation data.

Keywords: Radio occultation; Radio holography; Refraction; Ionosphere; Internal waves

1. Introduction

The effectiveness of radio occultation sounding of the atmosphere and ionosphere using the global positioning system (GPS) at wavelengths 19 and 24 cm has been demonstrated in many publications (Ware et al., 1996; Kursinski et al., 1997; Rocken et al., 1997; Feng and Herman, 1999; Schreiner et al., 1999). However, most publications do not concern the mesosphere-lower thermosphere (MLT) region

* Corresponding author. Institute of Radio Engineering and Electronics of Russian Academy of Sciences (IRE RAS), Fryazino, Vvedenskogo sq. 1, 141120 Moscow Region, Russia. Tel.: 7-095-526-92-61; fax: 7-095-203-84-14.

E-mail addresses: agp117@ire216.msk.su (A. Pavelyev), tsuda@kurasc.kyoto-u.ac.jp (T. Tsuda), igarashi@crl.go.jp (K. Igarashi), yueian@csrsr.ncu.edu.tw (Y.A. Liou).

1364-6826/03/$ - see front matter
PII: S1364-6826(02)00226-2

from 45 to 120 km due to the effects of F-layer when solving inverse radio occultation problem. Horizontal gradients owing to asymmetry of the ionosphere constitute a problem for inversion radio occultation data also. Modernized radio holography method (Pavelyev, 1998; Igarashi et al., 2000) can reveal fine structures in the ionospheric D-and E-layers. These structures may be connected with the internal waves influence observed by ground-based radars (Tsuda et al., 1990, 1994; Muraoka et al., 1988, 1998). Direct observation of internal waves in the mesosphere using radio occultation measurements may give new experimental data for understanding mechanisms of their propagation. The aim of this paper is to obtain new informations on the mesospheric parameters (features in the electron density distribution, temperature variations) by means of application of the radio holography analysis to radio occultation data.

1.1. The radio holographic method

Igarashi et al. (2000) described the basic principles of the radio holography application to analysis of GPS/MET radio occultation data. In the current state, the radio holography approach combines radar focused synthetic aperture principle and perturbation method. The focused synthetic aperture principle is applied for constructing reference beam using some knowledge of the average parameters of the atmosphere and ionosphere in the radio occultation region. Perturbation method is applied to the analysis of residuals in the phase and amplitude to find the deflections in the ionospheric and atmospheric parameters from the expected values.

Scheme of radio occultation experiments is shown in Fig. 1. The terrestrial atmosphere is modeled locally as spherically symmetric, with a local center of curvature O. One of the "ray paths" corresponding to the signals propagating from GPS to the low orbital satellite (LEO) (points G and P, respectively) lies in the plane of Fig. 1, which contains point O. This ray intersects the line PO at the angle β (Fig. 1) and has impact parameter p and corresponding refraction angle $\xi(p)$. The next connection exists between $\xi(p)$ and p for the case of spherical symmetry.

$$\beta = \pi + \xi(p) - \theta - \arcsin[p/(R_2)], \qquad p = R_1 \sin\beta. \quad (1)$$

Record of complex radio signals along the LEO trajectory is the radio hologram's envelope that contains the amplitude $A(t)$ and excess phase path $\psi(t) = kS_e(t)$ of the radio field as the functions of time. Temporal dependencies of the amplitude $A(t)$ and eikonal $S_e(t)$ are given in the GPS/MET radio occultation data. The functions $A(t)$ and $\psi(t)$ may be combined in the complex form:

$$E(t) = A(t)\exp[-i\psi(t)]. \quad (2)$$

A reference wave field $E_m(t) = A_m^{-1}(t)\exp[i\psi_m(t)]$, where $\psi_m(t) = kS_m(t)$ may be used to reveal the wave part of the radio hologram, where $A_m(t)$ and $\psi_m(t)$ are the expected amplitude and excess path for radio occultation region,

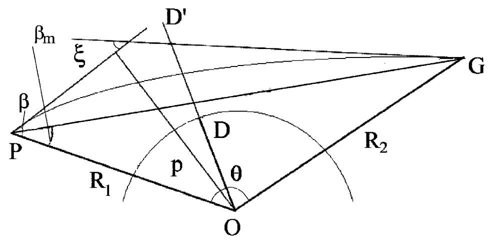

Fig. 1. Scheme of radio occultation. Radio occultation data are obtained by using a GPS transmitter and the "Micro-lab-1" satellite as a receiver (point P).

$k = 2\pi/\lambda$, λ is the wavelength of GPS/MET radio emission, and $S_m(t)$ is the eikonal (Kravtsov and Orlov, 1990). The ray corresponding to the phase function $\psi_m(t)$ begins in the point G and intersects the direction PO at angle $\beta_m(t)$ in point P (Fig. 1).

In the radio holography approach, the upper ionosphere influence may be accounted for directly by including in the phase of the reference beam $\psi_m(t)$. This may be done by means of using, for example, IRI-95 ionospheric model for a region and time of a radio occultation experiment. After multiplying both sides of Eq. (2) by the reference field $E_m(t)$, the wave part of the radio hologram $W(t)$ may be obtained

$$W(t) = E(t),$$

$$E(t) = A(t)A_m^{-1}\exp\{-i[\psi(t) - \psi_m(t)]\}. \quad (3)$$

The wave part $W(t)$ of the radio hologram contains only the phase and amplitude residuals connected with deflections of the refractivity vertical profile from the expected dependence included in the reference beam. Then, for analysis of the wave part of the radio hologram a perturbation method may be applied as described by Igarashi et al. (2000). The resulting refractivity altitude dependence may be presented as a sum of the expected profile and the wave part contribution (Igarashi et al., 2000).

As shown by Pavelyev et al. (2002), the next equations for angular $\Delta\beta$ and vertical Δh resolutions corresponding to the radio holographic method may be revealed for the case of circular orbits of GPS and LEO satellites:

$$\Delta\beta = \lambda/(2vT\cos\beta_m), \qquad \Delta p = \lambda R_1/(2vT);$$

$$\Delta h \approx \Delta p, \qquad v = R_1\, d\theta/dt, \quad (4)$$

where T is the time interval of coherent data handling, Δp is resolution in the impact parameter p. The vertical resolution Δh depends on the distance R_1, and does not include dependence on the angle β_m. The angular resolution $\Delta\beta$ diminishes when the angle β_m increases. The accuracy of the radio holographic method increases when v and T are growing and the wavelength is diminishing. The wavelength dependence of angular and vertical resolution, according to Eq. (4), is distinct from the Fresnel one: Δh, $\Delta\beta$ (radio holographic)$\sim \lambda$ and Δh, $\Delta\beta$ (Fresnel)$\sim \lambda^{1/2}$.

2. Analysis of the radio holograms of the ionospheric D- and E-layers

It is convenient to divide the wave part of the radio hologram into two independent amplitude and phase information channels. The amplitude channel is the main source for observing small spatial periods. The phase channel is more sensitive to long-scale vertical periods. The accuracy in resolution of the different spatial periods of wave structures is restricted in both channels by the vertical size of the radio hologram. To obtain the wave part of the radio hologram it is necessary to reveal the regular (low-frequency) part in the phase corresponding to reference beam for subsequent subtraction of influence of the upper ionosphere (mainly, F-layer) from experimental data as described by Igarashi et al. (2000). This may be done using the IRI-95 model describing the expected electron density profile for the time and place of radio occultation experiment. As shown by Igarashi et al. (2001), the high-frequency contribution of the quiet F-layer in the amplitude and phase variations is usually small (by factor of about 40 db) compared to the variations of the radio occultation signal due to perturbations in the E- and D-layer. Note also, that, according to Igarashi et al. (2001), the radio holography approach gives additional possibility to determine perturbed conditions in the upper ionosphere by analysis of the angular spectrum at two frequencies. This possibility was used to select the radio occultation events with quiet conditions in the F-layer and with sharp features in the limited height range corresponding to the D- and E-layers of the ionosphere. The coincidence of independent data at two frequencies gives one additional evidence for the D- or E-layer origin of strong variations in the radio occultation signal. The results of calculations of the phase of reference beam for frequencies $F1$ and $F2$ are given in Fig. 2 (left panel) for GPS/MET event 0393 (February 14, 1997; 13 h 56 m 23 s UT; 29.5 N 223.9 W). The excess phase path corresponding to the reference beam at two frequencies $F1$, $F2$ is described by the curves 1 and 3 in Fig. 2. The experimental data are shown by the curves 2 and 4 in Fig. 2. The results of calculations show good correspondence between the calculated and the experimental data. Deflections from the calculated curves are not higher than ± 1 cm in the height interval 65–112 km. The feature in the height interval 55–65 km may be connected with the influence of horizontal gradients in the ionosphere because the amplitude of deflections from regular contribution depends on the frequency, according to usual ionospheric square law. The horizontal gradients arose at the ray path turning point in the atmosphere—GPS satellite (evening part of the ionosphere). The results of restoration of the vertical distribution of the electron density for event 0393 are shown in Fig. 2 (right panel). The two maximums in the electron density are of about 15×10^9 1/m^3. Also the secondary maximums are seen in Fig. 2 (right panel). The results shown in Fig. 2 illustrate accuracy of radio holographic approach for solution inverse problem. The origin of this accuracy consists in independent construction of reference beam with subsequent application of perturbation method for retrieval of deflections in the experimental profile relative a model profile.

Another example of amplitude variations that corresponds to GPS/MET occultation event June 19, 1995, No. 0583 is shown in Fig. 3 (curves A1, A2, upper panel). The smooth

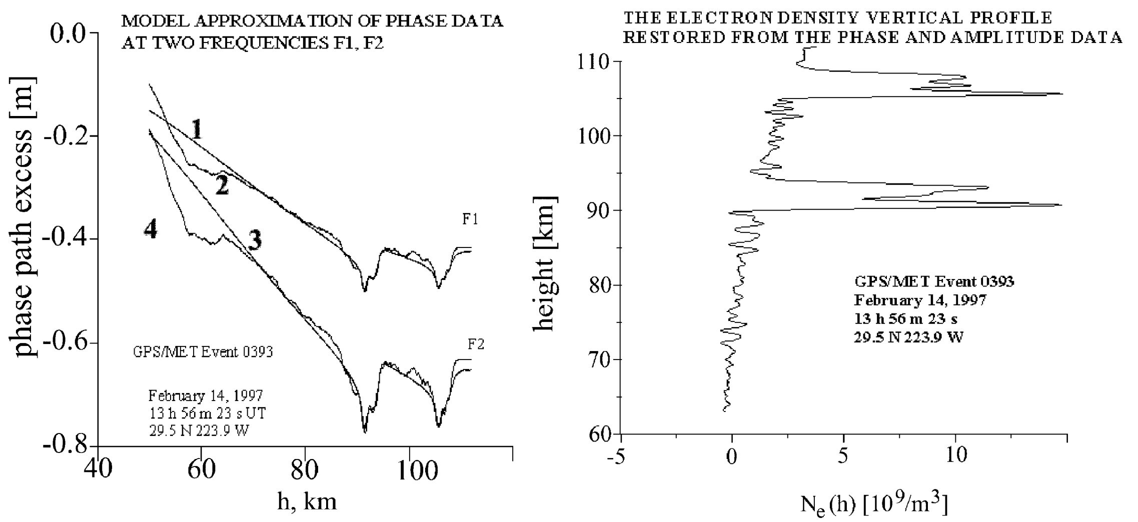

Fig. 2. Comparison of the phase of reference beam (curves 1 and 3 in the left panel) as function of the height with radio occultation phase excess data at frequencies $F1 = 1575.42$ and $F2 = 1227.6$ MHz (curves 2 and 4 in the left panel). The result of restoration of the vertical electron density distribution $N_e \times 10^{-9}$ (1/m^3) using radio holography approach (right panel).

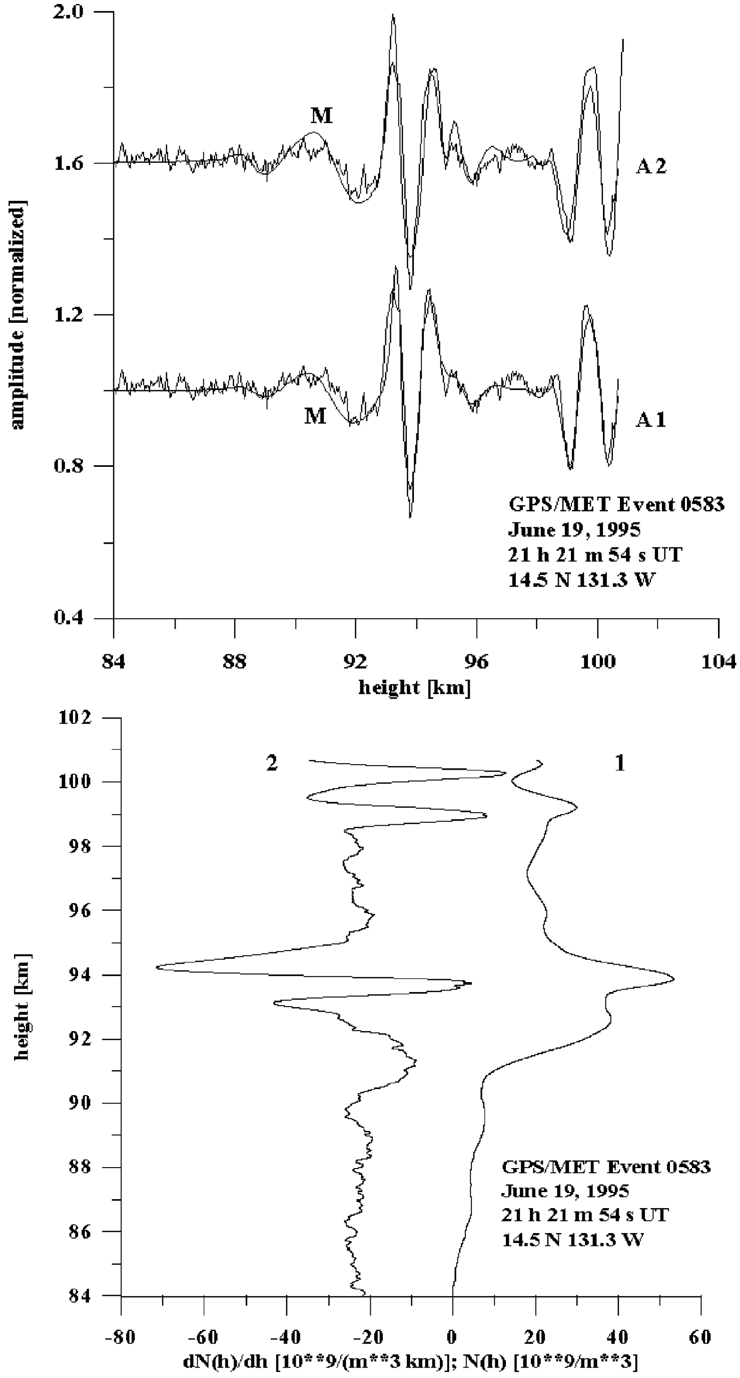

Fig. 3. Upper panel. Comparison of amplitude variations A1 and A2 at two frequencies with amplitude recalculated from restored electron density distribution (smooth curves m). Lower panel. Vertical distribution of the electron density $N(h)$ (curve 1) and its gradient $\mathrm{d}N/\mathrm{d}h$ (curve 2, displaced by 30×10^9 m^3 km^{-1}) retrieved from radio occultation data.

curves m in Fig. 3 show amplitudes of reference signal calculated using the model of electron density distribution. Amplitude variations A1, A2 are strongly correlated; their level is proportional to the ratio the f_2^2/f_1^2, thus indicating plasma's origin. In amplitude data influence of sporadic E-layer structure can be seen at heights 90–94 and 98–100 km. The

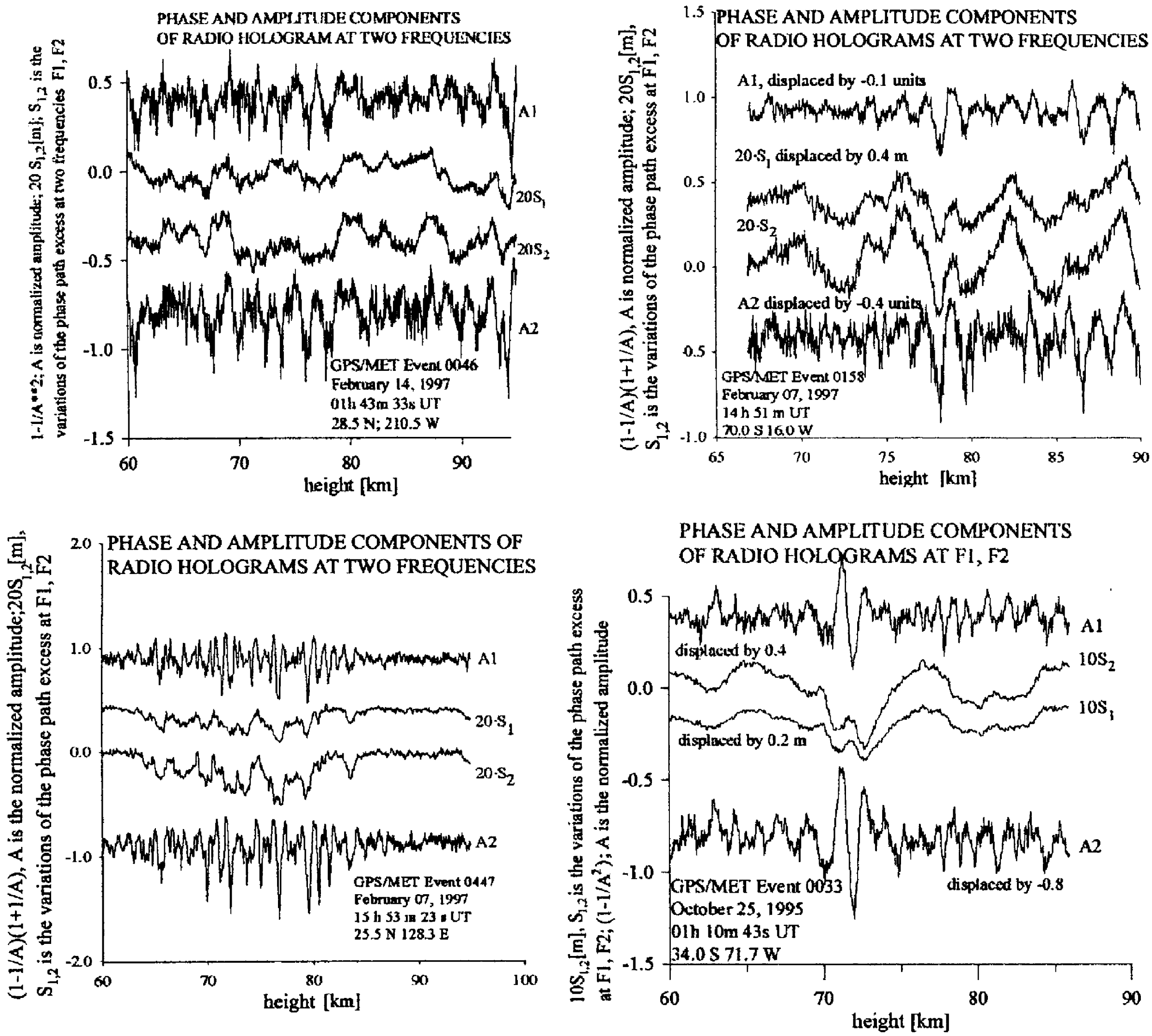

Fig. 4. Radio holograms of the D-layer of the ionosphere.

retrieved vertical profile $N_e(h)$ and vertical gradient $\mathrm{d}N_e(h)/\mathrm{d}h$ are shown in Fig. 3, lower panel, curves 1, and 2, respectively. Curve 2 is displaced by -30×10^9 m^{-3} km^{-1} for comparison with curve 1. Maximum value of negative gradient of about -45×10^9 m^{-3} km^{-1} is located at height 94.5 km (curve 2 in Fig. 3). The vertical profile $N(h)$ (curve 1 in Fig. 3) coincides with vertical gradient $\mathrm{d}N(h)/\mathrm{d}h$ (curve 2) indicating a feature at 94 km with a maximum of about 50×10^9 m^{-3}. As follows from the data in Fig. 3, analysis of information containing in amplitude channels of radio occultation signal gives detailed picture of vertical gradient distribution in the lower ionosphere. This is important because Earth-based tools usually give vertical profiles of the electron density distribution below maximum. Measurements of the vertical gradient of electron density are important for revealing different mechanisms of developing layered plasma's structures in the lower ionosphere.

The amplitude and phase components of radio holograms of the D-region of the ionosphere that correspond to four GPS/MET occultation events (February 14, 1997, No. 0046-left upper panel; February 07, 1997, No. 0447, 0158 - right upper and left lower panels; October 25, 1995 No. 0033 - right lower panel) are shown in Fig. 4. Occultation events No. 0046, 0447 took place near Japan (Okinawa) in the middle of daytime and in the middle of nighttime, respectively. The time-spatial coordinate of the main ray's minimal height H were close to 28.5°N 210.5°W, 01 h 43 m 33 s UT and 25.5°N 231.7°W, 15 h 53 m 23 s UT, correspondingly. The third event (February 07, 1997, No. 0158) corresponds to the summer daytime in the Antarctic region. The time-spatial coordinates of ray minimal height H varied from 71.2°S 18.2°W, $H = 95$ km, 14 h 51 m 05 s UT to 70.5°S 16.4°W, $H = 60$ km, 14 h 51 m 25 s UT. The fourth event takes place above the Andes Mountains region (South America) at 34.0°S 71.7°W, 01 h 10 m 43 s UT at the local evening time.

The two curves in the middle of panels in Fig. 4 correspond to the experimental excess phase variations at the first frequency $F1$, S_1 (upper curve), and at the second frequency $F2$, S_2, as functions of height. These curves have been multiplied and displaced to make more visible the variations that are connected with the wave structures. The upper ionospheric contribution was subtracted from the excess phase data by using the IRI-95 F-layer model for the time and region of radio occultation. The variations in amplitude (top and bottom pairs of curves in Fig. 4) are strongly correlated. The level of variations in the phase-path excess and in the amplitudes at the two frequencies is proportional to the ratio f_2^2/f_1^2, and this demonstrates that the variations originate due to fluctuations in the electron density.

The phase excess changes in the interval ±1 cm, with a random noise contribution of about ±1 mm. Spatial periods in the 1–3 km range can clearly be seen in the excess phase data of Fig. 4. A spatial period of 5 km can more clearly be seen in the excess phase data for Antarctic event than in the data for Okinawa events. In the amplitude data (top and bottom pairs of curves in Fig. 4) spatial periods in the 0.5–2 km range can also be seen. A feature at the height of 72 km (Andes event) and 78 km (Antarctic event) is seen in both the phase excess and amplitude data.

Analysis of Fig. 4 indicates that the amplitude data are more sensitive to high-spatial frequency components in the refraction index while the phase excess data are more sensitive to low-frequency components. These variations could correspond to wave structures in the electron density distribution in the D-layer of the ionosphere. The vertical gradient of electron density may be retrieved from the amplitude data by a method, which has been described by Igarashi et al. (2000). The results of the restoration $\mathrm{d}N_e(H)/\mathrm{d}H$ for four events 0033, 0046, 0447 and 0158 are shown in Fig. 5. For the ease of comparison, the curves have been displaced by 20×10^9 $(1/\mathrm{m}^3\ \mathrm{km}^{-1})$. The spatial periods for the Okinawan event are somewhat shorter by a factor of about two than the periods for other events. The amplitude of the waves over Okinawa is also greater, indicating a more intense process. The maximum value of the positive gradient is at a height of about 76 km. It follows from Fig. 5 that the wave structures in the D-layer seem to be quasi-sinusoidal with slow changes in the amplitude and frequency. This indicates the possible existence of only two-three propagated modes as was suggested by Sica and Russel, 1999, from analysis of the lidar data. For example, for the event 0033, the changes in the vertical period of the wave by two times from 2 to 1 km may be seen by comparing the vertical gradient of the electron density variations in the height intervals 65–70 and 74–79 km. The high amplitude values

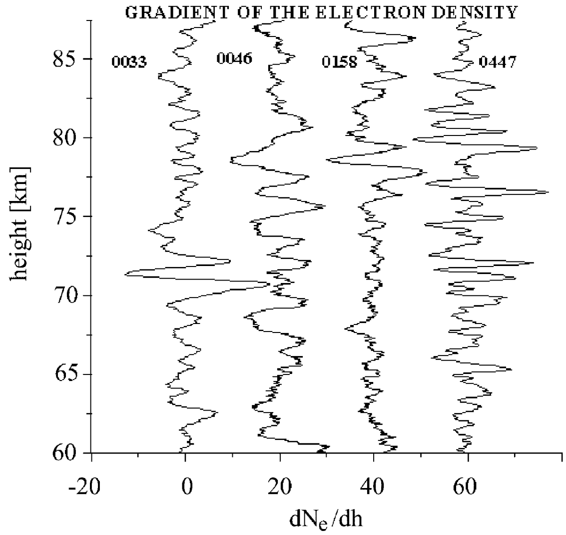

Fig. 5. Relative gradient of the electron density altitude distribution $\mathrm{d}N_e/\mathrm{d}h \times 10^{-9}$ $(1/\mathrm{m}^3\ \mathrm{km})$.

$\sim$ 8–10 $\times$ 10^9 $(1/\mathrm{m}^3\ \mathrm{km}^{-1})$ near 72 km (0033 event), 75–80 km (0046 event), 77–80 km (0158 event) and 66, 70–72, 77, 80 km (0447 event) may be connected with physical conditions of internal waves propagation. The strong features, which are seen in the height ranges 70–80 km (Okinawan event) and 75–80 km (Antarctic event), may correspond to breaking of internal waves in a region near the temperature inversion that is usually observed at this altitude by Earth-based radar and lidar tools (Hauchecorne et al., 1987). The perturbations observed in the vertical profiles of electron density might have a different origin. They may be connected with temperature waves caused by internal waves, whose amplitude grows with height.

The power spatial spectra of the vertical gradient of refractivity (N-units/km) that correspond to the variations in the gradients of electron density are shown in Fig. 6. The curves (displaced for ease of comparison by 40 db) show the separate power spatial spectra $W(2\pi/\Lambda)$ (expressed in $(\text{N-units})^2$), multiplied by 10^6, for all four events as a function of spatial frequency $2\pi/\Lambda$ (expressed in km^{-1}). A comparison of the four events reveal flat regions in the spatial spectrum with spatial periods between about 1.6 and 10 km. The straight lines in Fig. 6 show the slope of the spectra in the high-frequency region. The slope of the spectra in the high spatial frequency region and other parameters of the spectra are given in the Table 1.

The power degree in the high-frequency part of the spectrum is practically the same for all events (near $n_s = -3.$). The power degree for all events is very near to the slope in the tail spectrum of internal waves as described by Tsuda et al. (1991). So the variations in the electron density

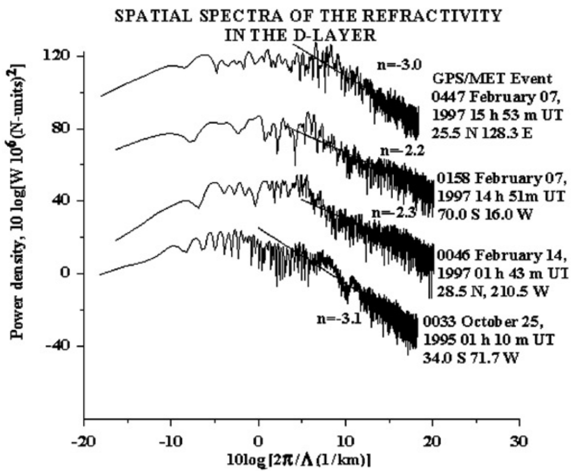

Fig. 6. Relative spatial spectra of waves in the D-layer of the ionosphere.

Table 1
Parameters of the spectra of the refractivity gradient in the D-layer

Number of event	Power degree, n
0447	-3.0 ± 0.3
0158	-2.2 ± 0.3
0046	-2.3 ± 0.3
0033	-3.1 ± 0.3

vertical profile may be connected with the influence of internal waves propagated in the neutral atmosphere.

3. Analysis of wind shear and internal wave mechanisms of plasma concentration

Observation of sharp features in the vertical electron density gradient in the D- and E-layer requires additional analysis of the possible cause of their origin. Two mechanisms of plasma concentration may be considered: wind shear and convergence in the neutral wind velocity field (Fig. 7). The first mechanism of plasma concentration is important in the upper part of the E-layer (at height of about 100–120 km) as described by Whitehead (1961), Kelley (1989), Mathews (1998). This effect arises due to Lorenz forces acting on the ions moving with velocities of 10–100 m/s with neutral gas in the horizontal direction (Fig. 7, panel A). Kelley (1989) introduced the simplified equation of motion for the plasma drift developing under the wind shear influence for the equilibrium case when acceleration of ions is absent:

$$W_{iz}(h) \approx a_i V_{\perp}; \quad a_i = \kappa_i/(1+\kappa_i^2)\sin\chi, \tag{5}$$

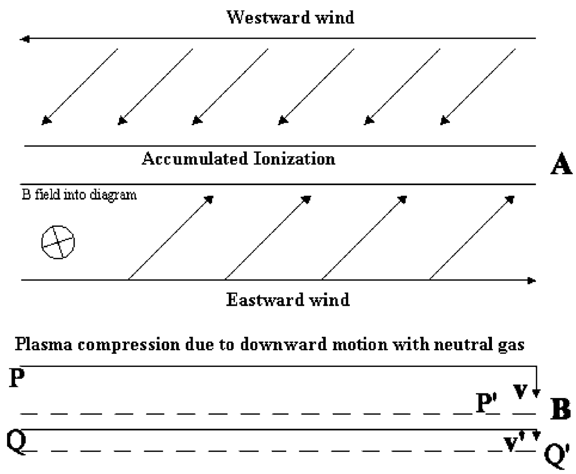

Fig. 7. Two mechanisms of plasma compression. A. Wind shear ion layer formation mechanism according to Kelley, 1989, Mathews, 1998. B. Ion layer formation due to convergence in the neutral gas velocity field. Downward velocity $\mathbf{v}$ of the upper boundary P is greater than the velocity $\mathbf{v}'$ of the lower boundary Q. After some time t the distance between the upper and lower boundary $P'Q'$ became lower than the initial distance PQ and plasma density increased. As shown by Beer, 1974, the convergence term is always present in the internal wave's velocity field and is equal to div $\mathbf{v} = v_t/\gamma H$, where v_t is the vertical perturbation velocity of the internal wave, γ is the ratio of specific heats under constant pressure and volume, H is the effective height of the atmosphere. Thus, internal waves with horizontal wavelength greater than 100 km and with vertical perturbation velocity of about 1 m/s may produce plasma layers in the lower ionosphere, which may be observed by the radio occultation method. The vertical size of plasma layer depends on the vertical wavelength of internal waves.

where $W_{iz}(h)$ is the vertical velocity of ions, κ_i is the ratio of the ions gyro frequency eB/M_i to the collision frequency v_{in}, M the molecular mass of ions, $V_{\perp}$ is the horizontal wind velocity component, which is perpendicular to the projection of the Earth's magnetic field on the horizontal plane, B is the magnitude of the Earth's magnetic field, χ is the angle between the Earth's magnetic field and vertical direction, e is the module of the electron charge.

For description of plasma compression effect owing to vertical motion of ions in the wind shear, one might solve the continuity equation:

$$\partial \ln \rho(h,t)/\partial t + W_{iz}(h)\partial \ln \rho(h,t)/\partial h = -\mathrm{d}W_{iz}(h)/\mathrm{d}h, \tag{6}$$

where $\rho(h,t)$ is the plasma density vertical distribution. Two terms in the left part of Eq. (6) describe the plasma advection. For plasma concentration the term in the right part of (6) is most important. Eq. (6) may be solved if the initial altitude plasma density distribution $\rho_0(h,0)$ corresponding to the time instant $t=0$ is known. For description of the wind shear effect, one may suppose a vertical distribution of the horizontal wind velocity and the vertical ions velocity

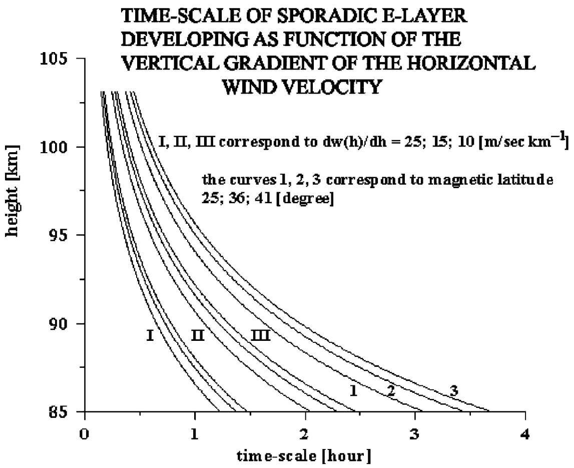

Fig. 8. The time-scale of plasma layer developing under influence of the wind shear effect.

in the form

$$V_\perp = V(h)T(t); \qquad W_{iz}(h) = w(h)T(t);$$

$$w(h) = a_i V(h). \tag{7}$$

It is assumed that the function $T(t) = 0$ if $t \leqslant 0$. So the wind shear effect begins at the time instant $t = 0$ under arbitrary dependence of the horizontal wind velocity on time t. It is convenient to introduce for solution (6) a new time variable τ:

$$\tau(t) = \int_0^t \mathrm{d}t T(t), \qquad \mathrm{d}\tau/\mathrm{d}t = T(t), \qquad \tau = 0, \text{ if } t = 0. \tag{8}$$

Solution of the Eq. (6) may be expressed in the form

$$\rho(h,\tau) = \rho_0[h_0(h,\tau),0]w[h_0(h,\tau)]/w(h), \tag{9}$$

where the function $h_0(h,\tau)$ might be found from the equation

$$\tau = \int_{h_0}^h \mathrm{d}h/w(h). \tag{10}$$

Direct substitution of (9) and (10) in (6) gives identity. Eqs. (9) and (10) gives a general solution of the continuity equation (6) ascribing the wind shear effect. According to (9) and (10) the plasma compression effect exists only owing to changes in the vertical ions velocity for the case of uniform plasma density initial distribution when $\rho_0(h,0) = \text{const}$. The time-scale of plasma layer developing may be described by the parameter $\tau_{sc} = 1/|\mathrm{d}a_i V_\perp/\mathrm{d}h|_{\max}$, where $|\mathrm{d}V_\perp/\mathrm{d}h|_{\max}$ is the maximal value of the vertical gradient of horizontal wind velocity. The results of calculation of the parameter τ_{sc} are shown in Fig. 8. For calculations, the standard dependencies of the molecular mass of the ions and the collision frequency on the height given by Kelley (1989) were used for the magnitude of geomagnetic field equal to 2.5×10^{-5} T. The parameter τ_{sc} is expressed in hours and shown in Fig. 8 on the horizontal axis as function of height (km) for different values of the geomagnetic latitude and vertical gradient of the horizontal wind velocity. According to Fig. 8, the time-scale of the plasma layer developing increases from 0.3 to 0.5 h at the height 103 km to 1.2–3.5 h at the height 85 km. The time-scale also increases with geomagnetic latitude and may be large in the polar region $\sim$ 20–40 h. For estimating the vertical scale and the electron density distribution in the plasma layer developed owing to wind shear influence it is useful to consider a sinusoidal model of the vertical distribution of the horizontal wind velocity:

$$W_i(h) = W_c[1 + r\sin(2\pi h/\Lambda)];$$

$$h_s - \Lambda/2 \leqslant h \leqslant h_s + \Lambda/2; \qquad r = W_a/W_c, \tag{11}$$

where $\Lambda/2$, h_s are the vertical size and the height of wind shear, W_c, W_a are the constant component and amplitude of alternate component in the ions vertical drift velocity, respectively, r is the index of modulation of the ions vertical velocity caused by the horizontal wind altitude variations. As may be shown, the dependence of the plasma density $\rho(h)$ on height is described by the following equations:

$$\rho(z_n) = \rho_0(Z^2-1)/(Z^2 + 2Z\sin(2\pi h/\Lambda + \gamma) + 1), \tag{12}$$

$$\sin\gamma = (Z^2-1)^{1/2}/Zch\varphi/2;$$

$$Z = (1+2\eta)^{1/2}; \qquad \eta = 2/(r\omega t)^2 F(\varphi),$$

$$F(\varphi) = \varphi^2/[2(ch\varphi - 1)]; \qquad \varphi = \omega t(r^2-1)^{1/2};$$

$$\omega = 2\pi W_c/\Lambda. \tag{13}$$

As it may be seen from Eqs. (12) and (13) the maximum in the plasma density corresponds to $h_m = \Lambda(3\pi/2 - \gamma)/(2\pi)$ and its value is equal to

$$\rho(h_m) = \rho_0 Q; \qquad Q = 1 + \tau\{[\tau^2/4 + F(\varphi)]^{1/2} + \tau/2\}/F(\varphi),$$

$$\tau = 2\pi t/\Lambda |a_i V_\perp|_{\max}, \tag{14}$$

where τ is time-dependent dimensionless parameter. Eqs. (12)–(14) may be used for calculation of the plasma density vertical distribution under influence of the wind shear. The height distribution in the electron density and its vertical gradient are shown in Figs. 9 and 10 correspondingly. Curve 1 shows the initial uniform distribution. Curves 2–4 show the height distribution corresponding to different values of the vertical gradient of the horizontal wind velocities $\mathrm{d}V_\perp(h)/\mathrm{d}h$ equal to 5.0; 10.0; 16.0 m s^{-1} km^{-1}. The higher values of the parameter $\mathrm{d}V_\perp(h)/\mathrm{d}h$ correspond to sharp distribution on the height both in the electron density and its gradient. Thus, Figs. 9 and 10 give clear illustration of plasma's compression mechanism of wind shear, which may be responsible for developing sharp layers with high values of gradient of electron density in the D- and E-layer of the ionosphere. The maximum in electron density is disposed very near to the points where the vertical plasma velocity is equal to zero. So the wind shear influence caused

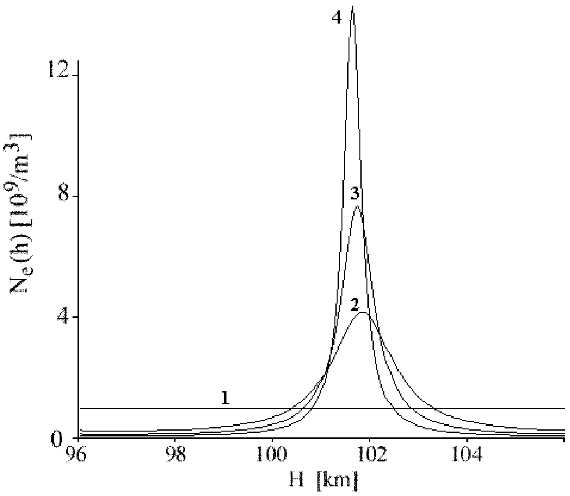

Fig. 9. Vertical distribution of the electron density $N_e \times 10^{-9}$ (1/m^3) due to influence of wind shear effect. The time of the wind shear developing is equal to 2000 sec. The curves 1, 2, 3, 4 correspond to the magnitude of the vertical gradient of horizontal wind equal to 0.0; 5.0; 10.0; 16.0 m s^{-1} km^{-1}.

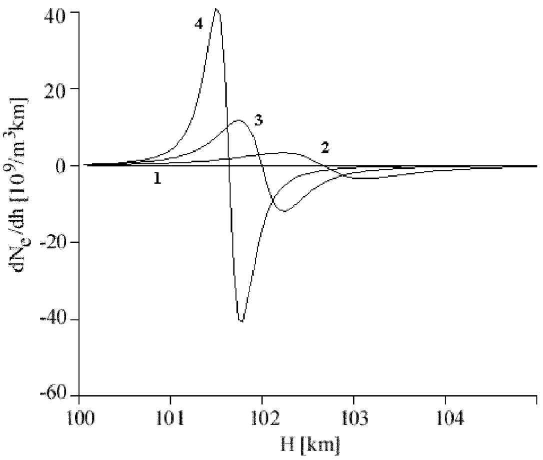

Fig. 10. Vertical distribution of the vertical gradient of electron density $dN_e/dh \times 10^{-9}$ (1/m^3 km) due to influence of the wind shear effect. The time of the wind shear developing is equal to 2000 s. The curves 1, 2, 3, 4 correspond to the magnitude of the vertical gradient of the horizontal wind equal to 0.0; 5.0; 10.0; 16.0 m s^{-1} km^{-1}.

an inhomogeneous distribution in the plasma density profile and also in the electron density vertical profile. This distribution depends in the first approximation on the time parameter τ (14). The time parameter τ determines a magnitude of maximum in the electron density Q relative to the background level because usually function $F(\varphi)$ is near to unity. If Q is known from radio occultation measurement, then the time parameter τ may be evaluated. For example, for the plasma layer shown in Fig. 2 the time parameter τ is equal to 3.8 (maximum below) and 2.4 (upper maximum). Usually the time of sporadic E-layer developing is about one hour as the Earth-based observations show (Kelley, 1989). This implies a possibility to evaluate the vertical gradient of the horizontal wind in the sporadic plasma layers revealed in Fig. 2. After substituting $t = 1$ h, $\tau = 3.8$; 2.4 in (14), the corresponding magnitudes $d_i V_\perp(h)/dh \approx 12$ m s^{-1} km^{-1} and 42 m s^{-1} km^{-1} may be obtained for the upper and lower layer in Fig. 2. These values correspond to usual vertical gradient of wind velocity observed in this region of the mesosphere from the Earth-based data (Titheridge, 1995). Titheridge (1995) also indicated that there exist diurnal variations in the height position of the winds in the mesosphere. This gives indirect evidence of slow coherent vertical motion of the neutral gas with long horizontal scale in the upper atmosphere.

Another mechanism of plasma layers developing may be connected with plasma's convergence effect in the neutral gas velocity field (Fig. 7, panel B). The neutral wind contains different contributions: background horizontal wind, changing with height, but constant in the horizontal directions, air motions in the horizontal and vertical directions connected with influence of long-scale tidal and planetary waves and internal waves as described by Beer, 1974. The effect of plasma convergence in the neutral gas, which is important for the interpretation of radio occultation data, is connected with altitude dependence of the vertical wind velocity (Fig. 7, panel B) (Beer, 1974). The spatial scale of coherence of vertical motion depends on the vertical and horizontal wavelength of an internal wave. For observed plasma layers in the mesosphere, the horizontal coherence scale of internal waves might be greater than 100 km. The vertical wavelength may be in the interval 1–20 km. For analysis of the connection between the plasma and neutral gas densities variations, plasma may be considered as a tracer, drifting with velocity of the neutral gas. The plasma and neutral gas flow may be described by continuity equations

$$d\{\ln[\rho_p(x,y,z,t)]\}/dt + \mathrm{div}[\boldsymbol{V}(x,y,z,t)] = -S,$$

$$\boldsymbol{V}(x,y,z,t) = 0, \qquad t < 0, \tag{15}$$

$$d\ln[\rho_n(x,y,z,t)]/dt + \mathrm{div}[\boldsymbol{V}(x,y,z,t)] = 0, \tag{16}$$

where $\rho_p(x,y,z,t)$, $\rho_n(x,y,z,t)$ are the plasma and neutral gas densities, respectively, expressed as a function of spatial coordinates x, y, z and time t, S is the factor of the plasma loss due to recombination processes in the neutral flow, $\boldsymbol{V}(x,y,z,t)$ is the plasma's velocity field supposed to be equal to the neutral gas velocity everywhere. It is assumed also that motion of the neutral gas initiated at the time instant $t = 0$ and the initial distribution of plasma density is equal to $\rho_p(x_0, y_0, z_0, 0)$. Eqs. (15) and (16) corresponds to the Lagrange's form, which shows changes of the density detected by an observer drifting with the plasma (or neutral gas) flow along a trajectory beginning in the arbitrary initial point $I(x_0, y_0, z_0, 0)$ and ending in the current point $P(x, y, z, t)$. Eqs. (15) and (16) have the same form and are independent of the different initial distributions of the plasma and neutral gas densities $\rho_p(x_0, y_0, z_0, 0)$, $\rho_n(x_0, y_0, z_0, 0)$. Comparing Eqs. (15) and (16) shows a possibility of excluding the divergence term $\mathrm{div}[\boldsymbol{V}(x, y, z, t)]$ by means of introducing the ratio of plasma and neutral gas densities $R(x, y, z, t)$:

$$R(x, y, z, t) = \rho_p(x, y, z, t)/\rho_n(x, y, z, t). \tag{17}$$

The continuity equation for the function $R(x, y, z, t)$ is more simple and has a form

$$\mathrm{d}\{\ln[R(x, y, z, t)]\}/\mathrm{d}t = -S. \tag{18}$$

Eq. (18) may be solved relative to the function $R(x, y, z, t)$ if the initial distribution $R(x_0, y_0, z_0, 0)$ is known:

$$R(x, y, z, t) = AR(x_0, y_0, z_0, 0);$$

$$A = \exp\left[-\int_0^t \mathrm{d}t\, S(x, y, z, t)\right], \tag{19}$$

where parameter A describes the tracer's loss (or income) on the path between the initial and current point I, P. Eq. (19) gives a general rule for any tracer moving with the neutral flow: ratio of the tracer and neutral gas densities is equal to its value in the initial position with coordinates $x_0, y_0, z_0, 0$ multiplied by factor A. This means that the tracer's density variations follow the changes of the neutral gas density along the flow. As a consequence of (19) the next connection exists between the neutral gas $\rho_n(x, y, z, t)$ and plasma densities $\rho_p(x, y, z, t)$:

$$\rho_p(x, y, z, t) = A\rho_n(x, y, z, t)\rho_p(x_0, y_0, z_0, 0) /\rho_n(x_0, y_0, z_0, 0). \tag{20}$$

Eq. (20) may be transformed by introducing the background neutral gas densities $\rho_b(x, y, z)$ which is assumed to be independent of the time t:

$$N_p(x, y, z, t) = N_d(x, y, z, t)G;$$

$$N_d = \rho_n(x, y, z, t)/\rho_b(x, y, z);$$

$$G = \rho_b(x, y, z)/\rho_n(x_0, y_0, z_0, 0),$$

$$N_p(x, y, z, t) = \rho_p(x, y, z, t)/[A\rho_p(x_0, y_0, z_0, 0)]. \tag{21}$$

The first part of equation (21) revealed direct proportionality between the plasma density variations $N_p(x, y, z, t)$ and the neutral gas density changes $N_d(x, y, z, t)$ at the fixed height h. The coefficient of proportionality, G, in (21) is equal to the ratio of the background neutral gas density $\rho_b(x, y, z)$ at the height h to the initial neutral gas density at the height $h_0\rho_n(x_0, y_0, z_0, 0)$. Actually, factor G in (21) may be evaluated from equation

$$G \approx \exp[-(h - h_0)/H], \tag{22}$$

where H is the effective height of the atmosphere. Eq. (22) is valid due to the exponential altitude dependence of the background neutral gas density in the atmosphere. Note that the factor G may be of about 2–6 if the difference h–h_0 is of about 0.8–1.8 H. Thus, factor G may be named as a gain showing increase in the plasma density due to downward motion of the neutral gas. Factor N_d in (21) describes the local changes in the neutral gas density at the fixed level with the height h. In the case of adiabatic process factor N_d may be expressed as function of the temperature variations in the neutral flow (Beer, 1974):

$$N_d = [T(x, y, z, t)/T_b(x, y, z)]^{1/(\gamma-1)};$$

$$N_p(x, y, z, t) = [T(x, y, z, t)/T_b(x, y, z)]^{1/(\gamma-1)}G, \tag{23}$$

where γ is the ratio of specific heat under constant pressure and volume, $\gamma \approx 1.4$, $T_b(x, y, z)$ is the background temperature of the neutral air. The second part of equation (23) connects the relative plasma density variations $N_p(x, y, z, t)$ with temperature variations in the neutral gas flow. Eqs. (20)–(23) have general importance because they describe the gain effect (increasing in concentration) for any tracer moving with the adiabatic neutral gas flow in the downward direction (for example, sodium, potassium, ozone and other minor constituents in the upper atmosphere). So the adiabatic neutral gas motion mechanism explains the plasma presence in the D-layer by advection process from the upper layers of the ionosphere caused by long-scale waves in the neutral air. The small-scale vertical plasma's density variations may be connected with internal waves having short vertical wavelength. Thus, analysis of the neutral gas motion mechanism revealed a possibility to connect the small-scale plasma density altitude variations with temperature changes in the D-layer. Also Eqs. (20)–(23) may be important for inverse problem solution, to determine the temperature variations in the mesosphere using measurements of the electron (or minor constituent) density $N_p(h)$:

$$T(x, y, z, t)/T_b(x, y, z) = C[\rho_p(x, y, z, t)]^{(\gamma-1)};$$

$$C = 1/[AG\rho_p(x_0, y_0, z_0, 0)]^{(\gamma-1)}. \tag{24}$$

Eq. (24) connects the temperature variations in the neutral gas with oscillations of the plasma density $\rho_p(x, y, z, t)$ for considered mechanism of plasma concentration in the D-layer of the ionosphere. The temperature variations are proportional to $\rho_p(x, y, z, t)^{(\gamma-1)}$, where $\rho_p(x, y, z, t)$ is the plasma density variations. The proportionality coefficient C depends on the initial (background) plasma distribution $\rho_p(x_0, y_0, z_0, 0)$, compression coefficient G and recombination losses in the neutral flow A. As it follows from this analysis, the magnitude of coefficient C depends on the long-scale vertical velocity of the neutral wind. If the long-scale vertical component of the neutral wind is absent,

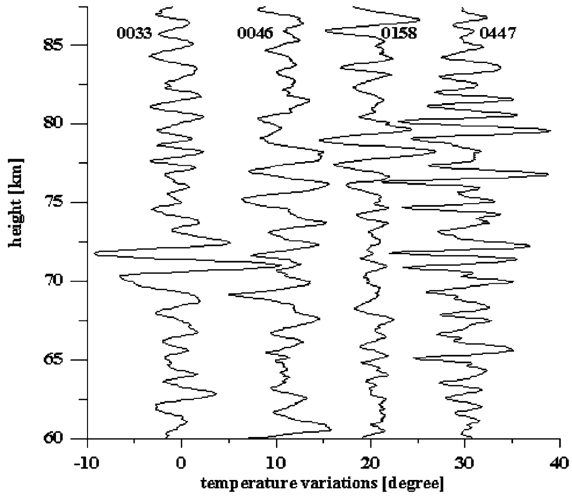

Fig. 11. Relative temperature variations in the D-layer of the ionosphere from radio occultation data.

then coefficient C depends only on the background distribution of the plasma density $\rho_p(x_0, y_0, z_0, 0)$ because $A = 1$, $G = 1$. Thus, if the coefficient C is known then absolute values of the temperature variations may be determined. If the coefficient C is unknown then only relative magnitude of the small-scale temperature variations may be determined.

The plasma density variations for four considered radio occultation events may be obtained by means of integrating the gradient of electron density (Fig. 5). However, the magnitude of the coefficient C is unknown, so only the relative temperature altitude distribution may be inferred from the radio occultation data. The results of revealing relative temperature variations from the measurements of the vertical gradient of the electron density profile (Fig. 5) are shown in Fig. 11 for four GPS/MET radio occultation events described above. For illustration the maximum of the positive temperature deflections is assumed to be 10°K for all events. This qualitatively corresponds to the amplitude of the temperature inversions observed by an Earth-based lidars tool at the considered altitudes. The curves 0046, 0158, 0447 are displaced by 10°K; 20°K; 30°K relative to the curve 0033 for convenience of comparing. The position of the maximums of temperature deviation corresponds to maximums in the electron density vertical profile and reveals strong features observed in the altitude distribution of the vertical gradient of the electron density profile (Fig. 5). The spatial size of the temperature features is about 1–2 km (about 0.8 km for 0447 event). The results of the provided analysis show the possibility of estimation position and size of the temperature inversion layers in the mesosphere region using radio occultation data. More detailed analysis of possible connections of the temperature and electron density altitude distribution in the D-layer is the task of future work.

4. Conclusion

The combined amplitude and phase analysis opened new possibilities for radio occultation observation wave structures in the lower ionosphere. The radio holograms of E- and D-layer of the ionosphere revealed wave structures with vertical periods of about 1–2 km in the altitude dependence of the electron density distribution. Theoretical analysis reveals the evidence of wind shear and internal wave effect on the origin of these structures. Due to this effect sharp maximums in the vertical distribution of the electron density may arise. The direct observation of the wave structures in the electron density vertical distribution in D-layer of the ionosphere opens new application of the radio occultation method for measuring parameters of the internal waves and the shape of the temperature vertical distribution in the mesosphere.

Acknowledgements

We are grateful to UCAR for access to the GPS/MET data. This contribution was prepared while one of the authors, Dr. A. Pavelyev, was visiting the Radio Science Center for Space and Atmosphere, Kyoto University, Kyoto, Japan. Dr. A. Pavelyev thus wishes to express his utmost gratitude to RASC. This work has been partly supported by the Russian Fund of Basic Research, Grant No. 01-02-17649.

References

Beer, T., 1974. Atmospheric Waves. Adam Hilger Ltd., London, 300 pp.

Feng, D.D., Herman, B.M., 1999. Remotely sensing the Earth's atmosphere using the global positioning system (GPS)-the GPS/MET data analysis. Journal of Atmospheric and Ocean Technology 16, 990–1002.

Hauchecorne, A., Chanin, M.L., Wilson, R., 1987. Mesospheric temperature inversion and internal wave breaking. Geophysical Research Letters 14 (9), 933–936.

Igarashi, K., Pavelyev, A., Hocke, K., Pavelyev, D., Kucherjavenkov, I.A., Matyugov, S., Zakharov, A., Yakovlev, O.I., 2000. Radio holographic principle for observing natural processes in the atmosphere and retrieving meteorological parameters from radio occultation data. Earth, Planets and Space 52 (11), 893–899.

Igarashi, K., Pavelyev, A., Hocke, K., Pavelyev, D., Wickert, J., 2001. Observation of wave structures in the upper atmosphere by means of radio holographic analysis of the radio occultation data. Advances in Space Research 27 (6–7), 1321–1327.

Kelley, M.C., 1989. The Earth's Ionosphere. Plasma Physics and Electrodynamics. Academic Press, New York, 1989, 484pp, ISBN 0-12-404012-8.

Kursinski, E.R., Hajj, G.A., Schofield, J.T., Linfield, R.P., Hardy, K.R., 1997. Observing Earth's atmosphere with radio occultation measurements using the global positioning system. Journal of Geophysical Research 102 (D19), 23429–23465.

Mathews, J.D., 1998. Sporadic E: current views and recent progress. Journal of Atmospheric and Terrestrial Physics 60 (4), 413–435.

Muraoka, Y., Sugiyama, T., Kawahira, K., Sato, T., Tsuda, T., Fukao, S., Kato, S., 1988. Formation mesospheric VHF echoing layers due to a internal wave motion. Journal of Atmospheric and Terrestrial Physics 30 (9), 819–829.

Muraoka, Y., Fukao, S., Sugiyama, T., 1998. Pre-sunrise mesospheric echoes and turbulent wind structure observed with MU radar. Geophysical Research Letters 25 (13), 2392–2396.

Pavelyev, A., 1998. On the possibility of radio holographic investigation on communication link satellite-to-satellite. Radioteknika i elektronika 43 (8), 939–944 (in Russian).

Pavelyev, A., Igarashi, K., Reigber, C., Hocke, K., Wickert, J., Beyerle, G., Matyugov, S., Kucherjavenkov, A., Pavelyev, D., Yakovlev, O.I., 2002. First application of the radio holographic method to wave observations in the upper atmosphere. Radio Science, in press.

Rocken, C., et al., 1997. Analysis and validation of GPS/MET data in the neutral atmosphere. Journal of Geophysical Research 102 (D25), 29,849–29,866.

Schreiner, W.S., Sokolovskij, S.V., Rocken, C., Hunt, D.C., 1999. Analysis and validation of GPS/MET radio occultation data in the ionosphere. Radio Science 34 (4), 949–966.

Sica, R.J., Russel, A.T., 1999. How many waves are in the internal spectrum? Geophysical Research Letters 26 (24), 3617–3620.

Titheridge, J.E., 1995. Winds in the ionosphere—a review. Journal of Atmospheric and Solar Terrestrial Physics 57, 1681–1714.

Tsuda, T., Kato, S., Yokoi, T., Inoue, T., Yamamoto, M., VanZandt, T., Fukao, S., Sato, T., 1990. Internal waves in the mesosphere observed with the middle and upper atmosphere radar. Radio Science 25 (4), 1005–1018.

Tsuda, T., VanZandt, T., Mizumoto, M., Kato, S., Fukao, S., 1991. Spectral analysis of temperature and Brunt–Vaisala frequency fluctuations observed by radiosondes. Journal of Geophysical Research 96 (D9), 17,265–17,278.

Tsuda, T., Murayama, Y., Nakamura, T., Vincent, R.A., Manson, A.H., Meek, C.E., Wilson, R.L., 1994. Variations of the internal waves characteristics with height, season and latitude revealed by comparative observations. Journal of Atmospheric and Solar Terrestrial Physics 56, 555–568.

Ware, R., et al., 1996. GPS sounding of the atmosphere from low Earth orbit—preliminary results. Bulletin of the American Meteorological Society 77, 19–40.

Whitehead, J.D., 1961. The formation of the sporadic-E layer in the temperate zones. Journal of Atmospheric and Solar Terrestrial Physics 20 (1), 49–58.